Scanning ultrafast electron microscopy

Ding-Shyue Yang, Omar F. Mohammed, and Ahmed H. Zewail[1]

Physical Biology Center for Ultrafast Science and Technology, Arthur Amos Noyes Laboratory of Chemical Physics, California Institute of Technology, Pasadena, CA 91125

Contributed by Ahmed H. Zewail, June 29, 2010 (sent for review June 1, 2010)

Progress has been made in the development of four-dimensional ultrafast electron microscopy, which enables space-time imaging of structural dynamics in the condensed phase. In ultrafast electron microscopy, the electrons are accelerated, typically to 200 keV, and the microscope operates in the transmission mode. Here, we report the development of scanning ultrafast electron microscopy using a field-emission-source configuration. Scanning of pulses is made in the single-electron mode, for which the pulse contains at most one or a few electrons, thus achieving imaging without the space-charge effect between electrons, and still in ten(s) of seconds. For imaging, the secondary electrons from surface structures are detected, as demonstrated here for material surfaces and biological specimens. By recording backscattered electrons, diffraction patterns from single crystals were also obtained. Scanning pulsed-electron microscopy with the acquired spatiotemporal resolutions, and its efficient heat-dissipation feature, is now poised to provide in situ 4D imaging and with environmental capability.

biological imaging | Schottky emission source | structural dynamics | nanomaterials imaging

The development of ultrafast electron microscopy (UEM) has enabled imaging in both space and time with atomic-scale resolutions (1, 2). The central concept involved is that of single-electron packets, which provide the high spatiotemporal resolutions due to the absence of the space-charge effect between electrons. Using femtosecond (fs) optical pulses, the electrons are generated from a LaB_6 photocathode and then accelerated typically to 200 keV. The time resolution is independent of the response of the video camera, as it is determined by the duration of the initial heating and electron pulses. With UEM, the different domains of electron microscopy were made possible: real-space imaging (3–5), diffraction (6–8), and electron-energy-loss spectroscopy (9, 10). Recent advances include 4D electron tomography (11), convergent-beam diffraction (12), and near-field electron microscopy (13).

SEM provides the unique capability of obtaining 3D-like images for materials surfaces (14–16). Moreover, environmental microscopy (17) can easily be invoked. Significantly, the electron source in SEM, a field emitter with a tip dimension of tens-to-hundreds of nanometers (nm), has higher brightness than that of the source in UEM (LaB_6), which has an active-area dimension of tens of micrometers (μm). Finally, the specimen is easier to handle; thick samples can be used and provide the means for heat dissipation, especially when the heating pulse is involved in dynamical studies.

Introducing ultrashort time resolution in SEM was not possible before, as in the past time-resolved studies were made by "chopping" the electron beam through the technique of high-frequency (MHz or GHz) beam deflection and blanking (18, 19). The temporal width of an electron pulse was hundreds of picoseconds (ps) and the overall resolution of the system was on the order of 10 nanoseconds (ns) (19). The main application of this methodology was in the study of the response of microelectronic devices or circuits under variation of the voltage applied; the vibrational mechanics of microstructures under the influence of varying voltages was also examined (20). Recently, spectroscopic detection of cathodoluminescence was resolved in the studies of carrier dynamics with 50 nm and 10 ps spatiotemporal resolutions (21, 22). For these studies, the electrons interacting with the specimen were responsible for the luminescence that was detected by a streak camera.

The concept of scanning ultrafast electron microscopy (SUEM) is entirely different in that the spatial resolution is that of SEM and the time resolution is determined by the ultrashort pulses involved, not by the deflection rate (19) or the streak camera used for optical detection (21). Unlike in the latter case where the electron pulse induces the carrier excitations, in SUEM, the electron pulses are the probes for imaging through the resultant secondary electrons. In this regard, the scheme of pump-probe is similar to that used in UEM (1) but with a different detection mechanism, a pixel-by-pixel recording rather than parallel processing of the image. Some key differences, however, do exist. Besides the scanning mode of operation, the observed signals in SUEM are obtained in the form of secondary or backscattered electrons, which are mainly the result of inelastic scattering.

Another difference is in the observed diffraction. Bragg spots or Debye–Scherrer rings, which are the dominant features of UEM diffraction, are replaced by Kikuchi lines (15, 23) when electron backscattering diffraction (EBSD) patterns are recorded in SUEM. As such, they are useful in resolving the structural evolution in a crystalline grain or domain along different crystallographic directions. Lastly, from a technical point of view, our current SUEM has a zirconium-oxide-coated sharp tungsten tip, which is a Schottky-emission gun in the relatively low-fluence regime (reaching field emission in the high-fluence limit) that is different from the LaB_6 tips used in the first and second generations (UEM1 and UEM2) in this laboratory. When operated in the conventional continuous emission mode (hereafter referred to as the SEM mode), these field-emission sources are known to be orders of magnitude higher in brightness (10^{11}–10^{12} $A/m^2/sr$) than LaB_6 (15). Thus, the advance in ultrafast imaging is significant for the further improvement of the source's coherence width (1).

Here, we report the first results obtained in SUEM. The source emitter is side-illuminated by a focused fs pulse of well-defined polarization, and the photoemitted electron pulse is the probe in imaging and diffraction recordings. Applications are demonstrated for biological and nanostructured materials over a wide range of magnification. Using the pulsed electrons in SUEM, diffraction patterns, obtained by detecting the backscattered electrons, were also recorded for a silicon wafer, and indeed the patterns display the Kikuchi lines. From these initial results, we expect the technique to open up various applications, as in UEM, but with the additional capability of scanning surfaces and the environmental microscopy mode.

Results and Discussion

SUEM and the Systems Imaged. The conceptual design of SUEM is depicted in Fig. 1*A*, which illustrates the integration of a fs laser system to a generic column with a field-emission source design. The optical system is a high-power fiber laser system that oper-

Author contributions: D.-S.Y., O.F.M., and A.H.Z. performed research and wrote the paper.

The authors declare no conflict of interest.

[1]To whom correspondence should be addressed. E-mail: zewail@caltech.edu.

ates at variable repetition rates, from 200 kHz to 25.2 MHz. The laser delivers fs infrared pulses with an average power of up to ~20 W; the wavelength is centered at 1030 nm and the pulse width is less than 300 fs. This infrared output is frequency doubled and tripled (or quadrupled) in a set of two nonlinear β-BaB_2O_4 crystals: the 515 nm pulses could be used in dynamics initiation in the specimen, whereas the 343 nm (or 257 nm) pulses are used for the generation of the electron pulse train. The ultraviolet light is separated and directed by dichroic mirrors, and tightly focused by a 125 mm focal lens onto the tip of the electron emitter (see below). At 25.2 MHz, the average pulse energy of the ultraviolet beam reaches ~2 nJ, before entering the microscope, resulting in an energy density of $F_{\text{laser}} \sim 1\ \text{mJ/cm}^2$ at the emitter tip.

The basic scanning mechanism of SEM was utilized with the electron acceleration voltage of up to 30 kV. As mentioned earlier, the cathode is a zirconium-oxide-coated tungsten [ZrO_x/W(100)] tip of several hundred nm in diameter. The work function is lowered by the ZrO_x coating from 4.5 eV to ~2.8 eV at high temperatures (16, 24–26). In the presence of an electrostatic field of $|\boldsymbol{E}_{\text{DC}}| \sim 10^7$ V/cm, the effective work function is further lowered by ~1.2 eV to $\phi_{\text{eff}} \sim 1.6$ eV (i.e., the Schottky effect); see below. Thus in this extended Schottky (thermionic, field-emission) regime (24, 25), electrons at a temperature of 1800 K (filament current of 2.48 A) can overcome the barrier, with some contribution from the tunneling effect, which is dominant in the field-emission regime for which the potential barrier width is considerably reduced.

In the SUEM mode, the filament current is completely turned off to suppress the background emission from the source at elevated temperatures. In the original design of the electron column, a pyrometrical window was introduced for viewing the glowing emitter and measuring its temperature remotely. The same window becomes a convenient entry port for the light pulses, defining the configuration of side-illumination of the emitter (Fig. 1*B*). At room temperature, the work function of the ZrO_x/W(100) tip is believed to be different and may be as high as that of tungsten in the absence of $\boldsymbol{E}_{\text{DC}}$ (27). As a result, the photon energy is higher than the work function of the cold emitter (lowered by ~1.2 eV due to the Schottky effect) by a small fraction (~0.3) of an eV for the 343 nm excitation. Therefore, electrons overcome this energy barrier through the absorption of the ultrafast photons, and not by the thermal effect, as demonstrated below.

Polarization of the ultraviolet beam is adjusted relative to the tip axis through a half-wave plate to maximize the pulsed current. The photoelectron trajectories follow the pathways that are defined by the components of the electron optics, and, as in SEM, they are the condenser lenses, stigmator, scan coils and the objective lens (Fig. 1*A*). After exiting the polepiece and entering the specimen chamber, the focused pulsed electron beam is directed by the scan coils and rasters across a specified region of the specimen to form an image (Fig. 1*C*).

The image construction is achieved through the scanning process with a well-defined dwell time for each beam location. It is the result of mapping over discrete pixels in the information space, thus forming a one-to-one correspondence with the set of beam locations on the specimen. The electron-matter interaction results in various types of signals, such as secondary and backscattered electrons as well as X-rays, and these are recorded by different detectors (15, 16). Here, we present secondary-electron images obtained by a positively biased Everhart–Thornley detector, and EBSD patterns recorded by a high-sensitivity digital camera.

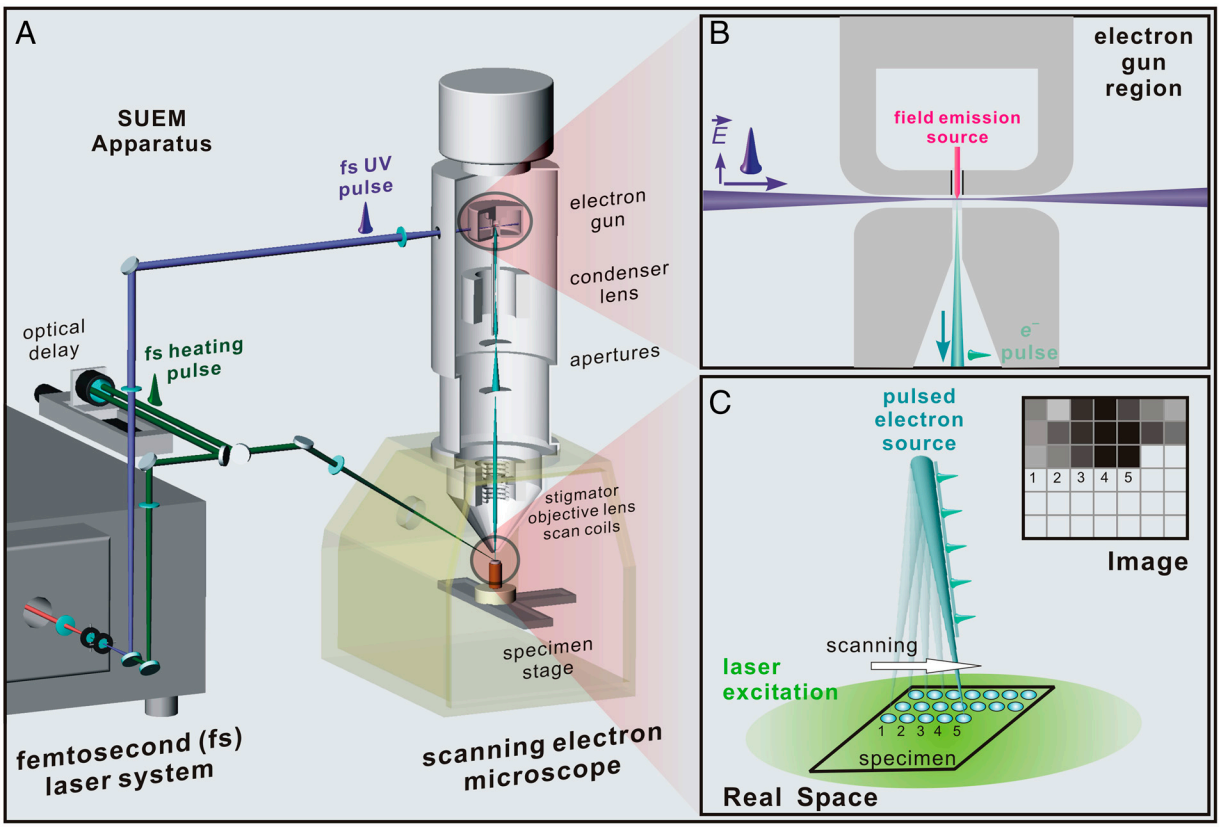

Fig. 1. Scanning ultrafast electron microscopy (SUEM), a conceptual schematic. (*A*) The interface of a femtosecond laser system to a modified SEM. (*B*) A close-up view of the field-emission region. Side-illumination of the field emitter by fs ultraviolet pulses is used for the electron generation. (*C*) A close-up view of the probe region and schematic for the pixel-by-pixel image construction. The axis of time is introduced by adjusting the arrival time of the laser excitation pulse at the specimen relative to that of the electron probe pulse using a variable optical delay line.

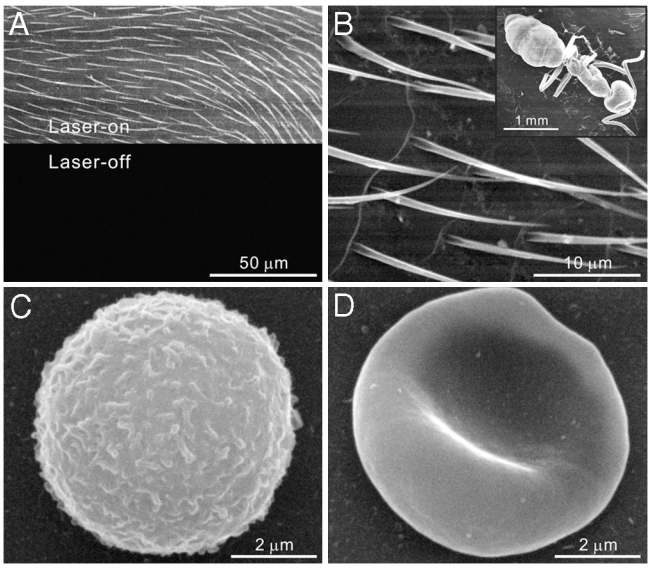

Fig. 2. SUEM images of biological specimens. (*A*) Image of setae on an ant's body at a magnification of 1,000× from a laser-on scan (*Upper*). A laser-off scan of the same region (*Lower*) shows the negligible background intensity. (*B*) The setae at a magnification of 5,000×. (*Inset*) An SUEM image at a magnification of 55×. (*C*, *D*) Images of a leukocyte (white blood cell) and an erythrocyte (red blood cell), respectively, at a magnification of 20,000×. Sub-μm features on the cell surfaces are clearly resolved.

To initiate a dynamical change in the specimen, as in UEM (1, 2), a clocking pulse must be introduced. In SUEM, a second window was included to permit the entry of such pulses into the chamber, and an optical delay stage was used for the control of the arrival times of the initiating and electron pulses at the specimen (Fig. 1*A*). For the first set of studies reported here, we focus on the feasibility of obtaining such images and diffraction patterns, and in future work we will address the time dependence in a similar manner to that of UEM.

The specimens imaged include: an ant; leukocytes (white blood cells) and erythrocytes (red blood cells) coated with a silver layer of a few nm thickness (by vapor deposition); uncoated multiwalled carbon nanotubes suspended on a copper grid (13); and aligned zinc oxide nanowires grown on a substrate (28). The EBSD patterns were from a crystalline Si(001) wafer with a thin layer of native oxide. To address the mechanism of photoelectron emission, measurements of the probe current at different pulse intensities were also made using a Faraday cup (connected to a picoammeter) that is placed at the specimen position.

SUEM Images and Diffraction Patterns. Shown in Figs. 2 and 3 are SUEM images recorded using the secondary electrons from the specimens. The fs pulses at 25.2 MHz were typically 2 nJ in energy and have a wavelength of 343 nm. The images were obtained either as a single frame with a dwell time of 200 microseconds (μs) at each pixel, or as integration of 64 frames with the dwell time being 3 μs. This integration suppresses image intensity fluctuations. Effectively, for each pixel, ∼5,000 pulses were utilized in the SUEM mode, resulting in an acquisition time of ∼50 s when an array of 512 × 442 pixels was scanned. The SUEM-EBSD patterns of Si(001), shown in Fig. 4, were recorded at a 70° tilt for a fixed point (no scanning involved); for this case, 10 nJ, 343 nm fs pulses at 12.6 MHz were utilized for the photoelectron generation and the acquisition time of ∼1 minute was typical for these recordings.

A critical test of SUEM imaging was made in the following way. With the field emitter being operated in the cold condition (at room temperature and not at 1800 K), the fs laser pulses were blocked/unblocked to observe changes in the image. As demonstrated in Fig. 2*A*, only black contrast was observed when the electron-generating fs pulses were blocked, which attests to the negligibility of both the thermionic and field tunneling emission from the unilluminated cold source. In addition, by changing the dwell time from a μs to as short as 50 ns, the response in intensity change (between laser-on and laser-off) remained instantaneous, indicating the absence of a "thermal tail" in the electron pulse train. Thus, the SUEM images obtained are indeed from the optically generated electrons, and in this mode of operation the images in Figs. 2 and 3 were acquired. The good image quality (Fig. 2*B*) reflects a steady probe current during the single-frame image acquisition with the pulsed electron source. It will become necessary to maintain such stability; i.e., a precise and stable alignment of the optical beam that is tightly focused on the sharp emitter tip, for an extended period of time over which dynamical studies can be made.

At high magnifications, carbon nanotubes and zinc oxide nanowires were imaged, as shown in Fig. 3. After a linear adjustment of image brightness and contrast, a good comparison between the SEM and SUEM images (all acquired through the 64-frame integration method) is evident; features of a few tens of nm were readily resolved. These results were achieved despite

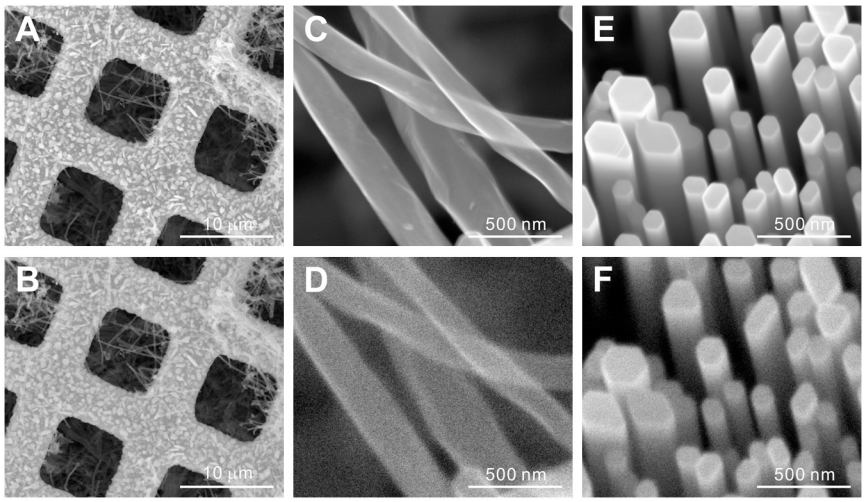

Fig. 3. SEM (*Upper*) and SUEM (*Lower*) images of nanostructures. (*A*, *B*) Carbon nanotubes on a copper grid imaged at a magnification of 5,000×. (*C*, *D*) Carbon nanotubes at a magnification of 100,000×. (*E*, *F*) Zinc oxide nanowires at a magnification of 100,000×. The SUEM and SEM images show similar contrast, and the spatial resolution is near 10 nm.

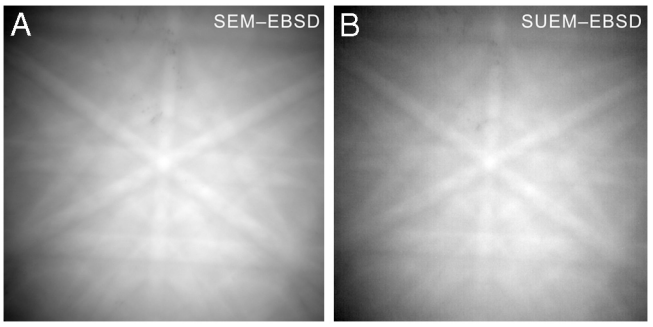

Fig. 4. Electron backscattering diffraction patterns of Si(001). Recorded in (*A*) the SEM and in (*B*) the SUEM (with 2×2 binning) modes used. The zone axis at the center is [111].

the fact that we have not fully optimized the stability of the fs pulse footprint on the emitter and without vibration isolation of the microscope. Such results may be more appreciated when realizing that the average probe current in the SUEM mode was only $10^{-2} \sim 10^{-5}$ of that used in the various typical settings of SEM. Given the threshold relationship (15) between the probe current and frame time, for a given contrast, higher resolution can be achieved by varying the acquisition time, repetition rate and image averaging of frames. We note that high repetition rates in SUEM are possible because of the more efficient (than UEM) heat dissipation. Thus, the limit in this case is the relaxation time under study.

The EBSD patterns of Si(001) are shown in Fig. 4, where the zone axis at the center is [111]. The close resemblance between the two images taken with the pulsed and continuous electron sources is evident. The major difference was the acquisition time, which is typically on the order of 10–100 ms for the SEM mode and tens of seconds for the SUEM mode at the operating laser characteristics. The three orders-of-magnitude difference matches well the ratio of the probe currents reaching the specimen. Previous time-resolved crystallographic work from this laboratory has demonstrated the usage of sub-ps pulses of ~500 electrons for tens of seconds per frame at the repetition rate of 1 kHz (29), and of $10 \sim 100$ electrons for seconds per frame at 200 kHz (30, 31). Given the high repetition rate (12.6 MHz) used in the experiments, we expect to extract information about time-dependent structural changes from Kikuchi patterns that are recorded using only several electrons per pulse, but in a similar acquisition time.

Mechanism of the Field Photoemission. The results of SUEM imaging and diffraction show that the photoelectrons were generated from the emitter tip by the 343 nm (3.6 eV) or 257 nm (4.8 eV) light pulses (Fig. 5). At the laser repetition rate of 25.2 MHz and with the highest spot-size setting of the SEM, we measured an average probe current of ~10 pA generated by 2 nJ, 343 nm pulses, which corresponds to an average number of ~2.5 electrons per pulse reaching the specimen. In this low-power regime, a linear relation between the fs pulse energy and the number of electrons at the probe was found (Fig. 5*A*), indicating that the photoelectrons are generated by single-photon absorption of the 343 nm light (see below).

For a given fs pulse energy, the highest probe current was observed when the polarization of the light was parallel to the tip axis and a significantly reduced value was seen when the polarization was not aligned with this axis; the minimum value was reached when the polarization was perpendicular to the tip axis. This observation of photoelectron tip emission is consistent with previous reports (32–36), although details of the mechanism are different. The polarization effect can be attributed to an increase in the probability of photon absorption (due to the preferred optical excitation of surface electrons) (37) and/or the field enhancement ("lightning-rod") effect near the tip (38, 39) when the laser field is parallel to the tip axis. The latter effect is less

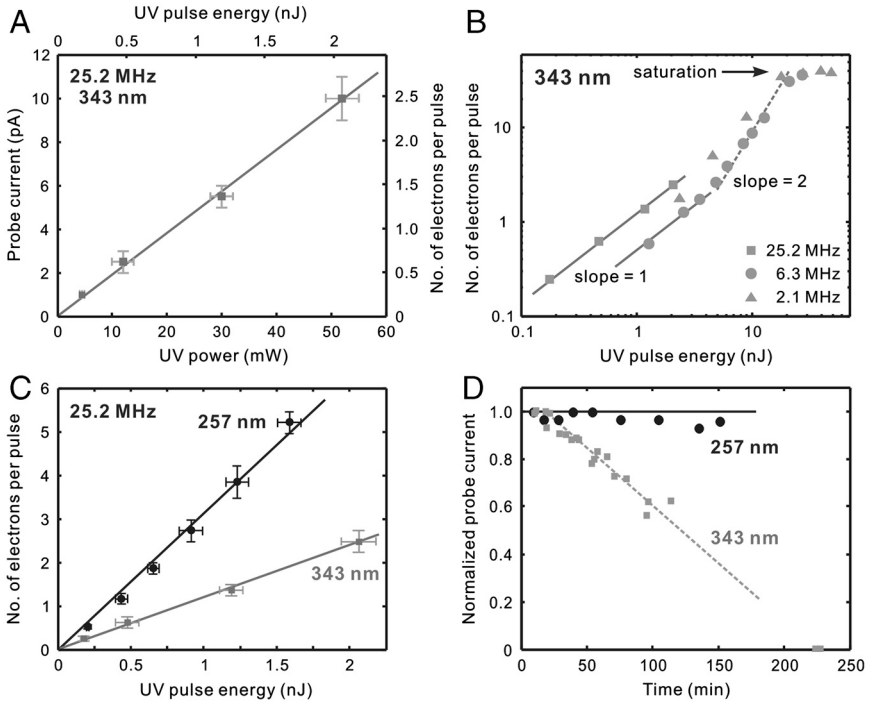

Fig. 5. Field-emitter dependence on pulse power. (*A*) A linear relationship between the number of electrons detected for the probe (n_p) and the 343 nm laser power used at the repetition rate of 25.2 MHz, in the low-power regime. (*B*) Dependence of n_p on the 343 nm pulse energy. A saturation behavior was noted at higher pulse energies. (*C*) A linear relation between n_p and the fs pulse energy, for both 257 nm and 343 nm light. The efficiency of photoemission by 257 nm is ~3.5 times that by 343 nm. (*D*) Photoemission efficiency from the cold emitter tip (by turning off the filament heating current) as a function of time lapse. A steady decay was seen in 2–3 hours for the case of the 343 nm light, whereas the decrease was negligible in 2.5 hours for the 257 nm case.

important when the wavelength of excitation becomes larger or comparable to the emitter's active length scale (13, 39).

The photon energy used here is higher than the work function for the cold $ZrO_x/W(100)$ tip and therefore, single-photon absorption by electrons is enough to produce photoemission on the fs time scale (35, 36). For a laser fluence of $F_{\text{laser}} \sim 1\ \text{mJ/cm}^2$, or a power density of $I_{\text{laser}} \sim 3 \times 10^9\ \text{W/cm}^2$ at the tip (more than an order of magnitude lower than that in ref. 32), the electric field $\boldsymbol{E}_{\text{laser}}$ imposed by this laser intensity [$|\boldsymbol{E}_{\text{laser}}| = 27.45\sqrt{I_{\text{laser}}}$ in SI units] is $\sim 10^6$ V/cm. This value is an order of magnitude smaller than the field strength imposed by the DC voltage ($|\boldsymbol{E}_{\text{DC}}| \sim 10^7$ V/cm), noting that such a field, $\boldsymbol{E}_{\text{DC}}$ or $\boldsymbol{E}_{\text{laser}}$, is much prominent when the tip size is sub-μm.

The relation between the total field strength $\boldsymbol{E}$ at the cathode and the effective work function ϕ_{eff} is given by (16)

$$\phi_{\text{eff}} = \phi_{\text{W}} - e\sqrt{\frac{e|\boldsymbol{E}|}{4\pi\varepsilon_0}} \equiv \phi_{\text{W}} - 3.8 \times 10^{-4}\ (\text{eV})\sqrt{|\boldsymbol{E}|}$$

where ϕ_{W} is the work function without field, e is the elementary positive charge, ε_0 is the vacuum permittivity, and $|\boldsymbol{E}|$ is in the unit of V/cm. The second term represents the Schottky effect; i.e., the lowering of the barrier by the induced field. Based on the value of $\boldsymbol{E}_{\text{laser}}$, relative to $\boldsymbol{E}_{\text{DC}}$, and our observation of the linear behavior shown in Fig. 5*A*, the mechanism of optical field emission (32) is believed to be less important in the present low-power regime. For $|\boldsymbol{E}_{\text{laser}}| \sim 10^6$ V/cm, ϕ_{eff} is further lowered by ~0.06 eV.

At higher pulse energies, we observed a deviation from the aforementioned linear relationship between the fs light energy and the probe current (Fig. 5*B*). A change in the value of the slope from one signifies the involvement of other mechanisms such as the simultaneous absorption of two or more photons in photoelectron generation (35) and, possibly, an increased contribution from field emission. Saturation was reached when the 343 nm fs pulse energy was ~25 nJ (at the lower repetition rates of 2.1 and 6.3 MHz), yielding ~40 electrons per pulse at the specimen. At this level, due to the relatively high number of photoemitted electrons (likely on the order of 10^4) at the source, the electron–electron repulsion at the emitter tip could contribute to spatial and temporal profile broadenings (40), which is consistent with our observation that resolution in the images decreases at the highest electron density used.

We also obtained images using the 257 nm pulses. For these pulses a higher efficiency (by a factor of ~3.5) in photoelectron generation was evident, compared to the 343 nm light (Fig. 5*C*). The same mechanism of single-photon absorption is involved in the low-power regime because of the linear relationship between the fs pulse energy and the number of electrons detected at the specimen. A similar saturation behavior was also noted when the pulse energy becomes above 15 nJ in value (measured at 6.3 MHz). However, there was one major difference in the performance. The photoemission efficiency by the 257 nm light remained at a similar level for much longer times (Fig. 5*D*). This is likely because photons with higher energy can assist electrons to overcome the elevated work function barrier even when the coverage of gas molecules occurs over time. Accordingly, the higher stability of the photoemitter performance with 257 nm fs pulses becomes especially suitable for dynamics studies that require longer acquisition times.

SUEM, the third generation in the development of UEM, is now poised for measurements of structural dynamics, particularly in various types of bulk or thicker specimens that are inappropriate for a transmission geometry. The repetition rates used for different experiments will be ultimately determined by the characteristic recovery time of the materials studied. The fs laser system provides flexibility for the time between pulses, but for SUEM this time could be reduced to the ns domain simply because of the use of thick samples. Finally, the axis of time on the ultrashort time scale is defined by adjustment, through a variable optical delay line as illustrated in Fig. 1*A*, of the arrival time of the laser excitation pulse at the specimen relative to that of the electron probe pulse.

Concluding Remarks. In this report, we presented the progress made so far in the development of scanning ultrafast electron microscopy at Caltech. In the scanning mode, an ultrashort electron pulse train was generated from a cold field-emission source and used for imaging and diffraction. With this SUEM, nanometer and sub-ps spatiotemporal resolutions are now achievable through the detection of secondary and backscattered electrons. The reported applications for various specimens at different magnifications demonstrate the capability of imaging 3D surface structures of materials and biological systems. Further extensions will include time-resolved investigations of elementary processes under environmental conditions, with focus on functional molecular assemblies (41) and biological dynamics (2).

ACKNOWLEDGMENTS. We thank Brett Barwick for the very helpful discussion and assistance during the design and operation of the microscope, especially in the initial stage. We also thank Lubomir Tuma, Michal Geryk, and Greg Schwind for exchange of information during the design stage of SUEM, and Tony Carpenter for all his effort in arranging for a timely installation in the laboratory. This work was supported by the Air Force Office of Scientific Research and the National Science Foundation in the Gordon and Betty Moore Center for physical biology at Caltech.

1. Zewail AH, Thomas JM (2010) *4D Electron Microscopy: Imaging in Space and Time* (Imperial College Press, London).
2. Zewail AH (2010) Four-dimensional electron microscopy. *Science* 328:187–193.
3. Park HS, Baskin JS, Kwon OH, Zewail AH (2007) Atomic-scale imaging in real and energy space developed in ultrafast electron microscopy. *Nano Lett* 7:2545–2551.
4. Kwon OH, Barwick B, Park HS, Baskin JS, Zewail AH (2008) Nanoscale mechanical drumming visualized by 4D electron microscopy. *Nano Lett* 8:3557–3562.
5. Flannigan DJ, Samartzis PC, Yurtsever A, Zewail AH (2009) Nanomechanical motions of cantilevers: Direct imaging in real space and time with 4D electron microscopy. *Nano Lett* 9:875–881.
6. Grinolds MS, Lobastov VA, Weissenrieder J, Zewail AH (2006) Four-dimensional ultrafast electron microscopy of phase transitions. *Proc Natl Acad Sci USA* 103:18427–18431.
7. Kwon OH, Barwick B, Park HS, Baskin JS, Zewail AH (2008) 4D visualization of embryonic, structural crystallization by single-pulse microscopy. *Proc Natl Acad Sci USA* 105:8519–8524.
8. Park HS, Kwon OH, Baskin JS, Barwick B, Zewail AH (2009) Direct observation of martensitic phase-transformation dynamics in iron by 4D single-pulse electron microscopy. *Nano Lett* 9:3954–3962.
9. Carbone F, et al. (2009) EELS femtosecond resolved in 4D ultrafast electron microscopy. *Chem Phys Lett* 468:107–111.
10. Carbone F, Kwon OH, Zewail AH (2009) Dynamics of chemical bonding mapped by energy-resolved 4D electron microscopy. *Science* 325:181–184.
11. Kwon O-H, Zewail AH (2010) 4D electron tomography. *Science* 328:1668–1673.
12. Yurtsever A, Zewail AH (2009) 4D nanoscale diffraction observed by convergent-beam ultrafast electron microscopy. *Science* 326:708–712.
13. Barwick B, Flannigan DJ, Zewail AH (2009) Photon-induced near-field electron microscopy. *Nature* 462:902–906.
14. Boyes ED (1998) High-resolution and low-voltage SEM imaging and chemical microanalysis. *Adv Mater* 10:1277–1280.
15. Goldstein JI, et al. (2003) *Scanning Electron Microscopy and X-Ray Microanalysis* (Springer, New York), 3rd Ed.
16. Reimer L (1998) *Scanning Electron Microscopy: Physics of Image Formation and Microanalysis* (Springer, Berlin), 2nd Ed.
17. Gai PL, Boyes ED (2003) *Electron Microscopy in Heterogeneous Catalysis* (IOP Publishing, Bristol, UK).
18. Plows GS, Nixon WC (1968) Stroboscopic scanning electron microscopy. *J Phys E Sci Instrum* 1:595–600.
19. MacDonald NC, Robinson GY, White RM (1969) Time-resolved scanning electron microscopy and its application to bulk-effect oscillators. *J Appl Phys* 40:4516–4528.
20. Ogo I, MacDonald NC (1996) Application of time-resolved scanning electron microscopy to the analysis of the motion of micromechanical structures. *J Vac Sci Technol B* 14:1630–1634.
21. Merano M, et al. (2005) Probing carrier dynamics in nanostructures by picosecond cathodoluminescence. *Nature* 438:479–482.
22. Corfdir P, et al. (2010) Exciton recombination dynamics in *a*-plane (Al,Ga)N/GaN quantum wells probed by picosecond photo and cathodoluminescence. *J Appl Phys* 107:043524.

23. Schwartz AJ, Kumar M, Adams BL, eds. (2000) *Electron Backscatter Diffraction in Materials Science* (Kluwer, Boston).
24. Tuggle DW, Swanson LW (1985) Emission characteristics of the ZrO/W thermal field electron source. *J Vac Sci Technol B* 3:220–223.
25. Fransen MJ, Faber JS, van Rooy TL, Tiemeijer PC, Kruit P (1998) Experimental evaluation of the extended Schottky model for ZrO/W electron emission. *J Vac Sci Technol B* 16:2063–2072.
26. Bronsgeest MS, Kruit P (2006) Temperature dependence of the work function of the Zr/O/W(100) Schottky electron source in typical operating conditions and its effect on beam brightness. *J Vac Sci Technol B* 24:887–891.
27. Tamura K, et al. (2005) Surface structure analysis of Zr-O/W(100) at high temperature by x-ray photoelectron diffraction. *Surf Interface Anal* 37:217–220.
28. Yang D-S, Lao C, Zewail AH (2008) 4D electron diffraction reveals correlated unidirectional Behavior in zinc oxide nanowires. *Science* 321:1660–1664.
29. Baum P, Yang D-S, Zewail AH (2007) 4D visualization of transitional structures in phase transformations by electron diffraction. *Science* 318:788–792.
30. Barwick B, Park HS, Kwon OH, Baskin JS, Zewail AH (2008) 4D imaging of transient structures and morphologies in ultrafast electron microscopy. *Science* 322:1227–1231.
31. Park HS, Baskin JS, Barwick B, Kwon OH, Zewail AH (2009) 4D ultrafast electron microscopy: Imaging of atomic motions, acoustic resonances, and moire fringe dynamics. *Ultramicroscopy* 110:7–19.
32. Hommelhoff P, Sortais Y, Aghajani-Talesh A, Kasevich MA (2006) Field emission tip as a nanometer source of free electron femtosecond pulses. *Phys Rev Lett* 96:077401.
33. Ropers C, Solli DR, Schulz CP, Lienau C, Elsaesser T (2007) Localized multiphoton emission of femtosecond electron pulses from metal nanotips. *Phys Rev Lett* 98:043907.
34. Ropers C, Elsaesser T, Cerullo G, Zavelani-Rossi M, Lienau C (2007) Ultrafast optical excitations of metallic nanostructures: From light confinement to a novel electron source. *New J Phys* 9:397.
35. Barwick B, et al. (2007) Laser-induced ultrafast electron emission from a field emission tip. *New J Phys* 9:142.
36. Hilbert SA, Neukirch A, Uiterwaal CJGJ, Batelaan H (2009) Exploring temporal and rate limits of laser-induced electron emission. *J Phys B-At Mol Opt* 42:141001.
37. Venus D, Lee MJG (1983) Polarization dependence of photoexcitation in photofield emission. *Surf Sci* 125:452–472.
38. Novotny L, Bian RX, Xie XS (1997) Theory of nanometric optical tweezers. *Phys Rev Lett* 79:645–648.
39. Martin YC, Hamann HF, Wickramasinghe HK (2001) Strength of the electric field in apertureless near-field optical microscopy. *J Appl Phys* 89:5774–5778.
40. Gahlmann A, Park ST, Zewail AH (2008) Ultrashort electron pulses for diffraction, crystallography and microscopy: Theoretical and experimental resolutions. *Phys Chem Chem Phys* 10:2894–2909.
41. Weiss PS (2008) Functional molecules and assemblies in controlled environments: Formation and measurements. *Acc Chem Res* 41:1772–1781.